Hindawi
Geofluids
Volume 2022, Article ID 5872889, 22 pages
https://doi.org/10.1155/2022/5872889

Research Article

Study on Movement Law of High-Position Thick and Hard Roof and Mine Earthquake Control by Ground Fracturing Technology

Yanbo Liang,[1] Yuanfang Cheng,[1] Zhongying Han,[1] Chuanliang Yan,[1] Xiufeng Zhang,[2] Chao Wang,[2] and Songcai Han[3]

[1]*School of Petroleum Engineering, China University of Petroleum (East China), Qingdao, 266590 Shandong, China*
[2]*Yanzhou Coal Mining Co., Ltd, Zoucheng, 273512 Shandong, China*
[3]*College of Energy Resources, Chengdu University of Technology, Chengdu, Sichuan, 610059, China*

Correspondence should be addressed to Zhongying Han; hzy_0218@163.com

Received 13 May 2022; Revised 6 June 2022; Accepted 8 June 2022; Published 29 June 2022

Academic Editor: Zhengzheng Xie

The field monitoring data showed that the fracture of high-position thick and hard roof (THR) was the main reason for the frequent occurrence of high-energy mine earthquake events (magnitude > 2.0) in the no. 6 mining district of Dongtan coal mine. In order to study the fracture characteristics of high-level THR and seek a reasonable and effective control method, taking the $63_{up}06$ working face as the engineering background, the FLAC model was built to simulate the strata movement law before and after fracturing. The simulation results showed that the THR first breaking span was 340 m, the tensile failure runs through the whole THR, and the subsidence increased rapidly when THR reached the first breaking span. The THR breakage is related to the continuous upward transfer of horizontal compressive stress, which results in the concentration of horizontal compressive stress in THR. After ground fracturing, the first breaking span of THR decreased, and different fracturing positions have a great impact on the THR fracture form. When the fracturing position is close to the center of the first breaking span, there is no large cantilever breaking form in the THR, the THR breaks on both sides of the top and sinks along the hydraulic fracture in the middle, and the collapse degree is relatively uniform. Then, the fracturing test was carried out in the $63_{up}06$ working face, the results showed that during the first 400 m of the $63_{up}06$ working face mining after fracturing, 702 microseismic events occurred in total, including 12 high-energy vibration events which include 4 mine earthquakes of magnitude 2.0 and 8 mine earthquakes of magnitude 1.0-2.0. Compared with the adjacent working face, the quantity of high-energy mine earthquake events in the $63_{up}06$ working face has been significantly controlled.

1. Introduction

The thick and hard roof (THR) above the coal seam is difficult to collapse in time because of its characteristics such as large thickness, high strength, and integrity [1–7]. This part of the rock stratum occurs outside the traditional basic roof, with a thickness of tens of meters or even hundreds of meters. The THR breakage releases a large amount of energy and is easy to induce the rock burst in the stope, which significantly threatens the mining safety production [8–13]. With the gradual transfer of coal mining to the deeper depth, the in situ stress is further increased, the geological conditions are more complex, and the problem of coal mine dynamic disaster will become more prominent [14–18]. Therefore, it is urgent to carry out the relevant research on the occurrence mechanism and prevention of coal mine dynamic disaster induced by the THR breakage.

In the study of fracture mechanisms of the THR, Xu et al. put forward the theoretical failure model of thick and hard rock strata to calculate the rock failure laws in Yangliu Coal Mine, Huaibei Coalfield, China. Then, the reliability of this model was verified by the methods of numerical simulation and surface subsidence measurement [19]. Based on the energy distribution formula of an elastic foundation beam, Liu et al. analyzed the accumulation and release of energy before and after the fracture of the key strata and considered that the nearer the working face, the greater the release energy of the rock beam [20]. Based on the long beam

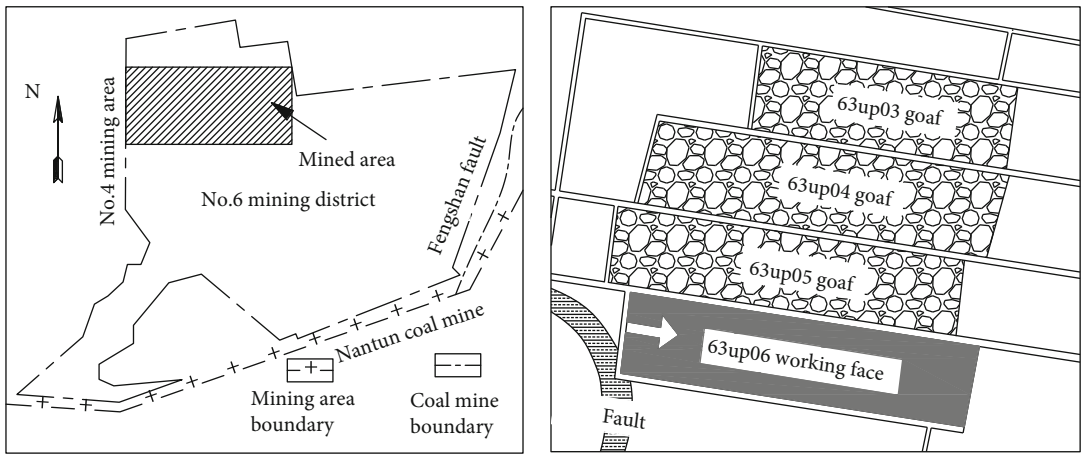

Figure 1: The location of the no. 6 mining district: (a) plan layout of the no. 6 mining district; (b) plan layout of the $63_{up}06$ working face.

theory, Zhao et al. calculated the first weighting characteristics and extreme fracture step distance and introduced a new technology called deep-hole presplitting blasting (DPB) which could break the THR by drilling holes with different depths and angles at different levels of roof rock and then blasting it [21]. Jia et al. established a thick-hard limestone roof cracking model and discussed the factors that affect roof fracture initiation and extension and found that roof fracture was developed in the stress concentration area below the upper coal face residual coal pillar [22]. Chen et al. developed a roof control scheme of advanced deep hole precracking using 3DEC software for the simulations. It was verified by comparing with the practical application results [23]. Zhang et al. proposed an elastoplastic plate model to study the dynamic elastic-plastic response characteristics of the roof, and the FLAC3D simulation was performed to analyze the failure process of dynamic stress on coal-rock mass [24]. Lan et al. employed an integrated method that included a borehole TV tester, borehole-based monitoring of strata movements, and monitoring of support resistance in the working face to analyze the fracture characteristics of the overlying rock layers and the strata behaviors [25]. The above studies all show that the THR breaking releases a large amount of energy, which threatens the safety production of coal mine. However, there are few studies on the fracture characteristics of high-position THR.

In terms of THR control technology research, Guo et al. proposed the new roadside support method with constant resistance yielding limit supporting under the hard roof, and the feasibility was verified by establishing the theoretical model and field practice [26]. Zhang et al. proposed a solid backfill method for controlling hard roof-induced face bursts and analyzed the interaction between the solid backfill body and the roof under different backfilling ratios [27]. Huang et al. proposed a control technology which involves drilling small aperture drill holes into the hard roof of the initial room with an anchor cable rig and performing hydraulic fracturing to control the hanging roof, based on the stress arch theory and the fracture mechanics [28]. Zhang et al. proposed the "ultradeep hole presplit blasting measure," the "large-diameter borehole pressure relief measure," and the "reducing advancing speed measure" to reduce the risk of rock burst, which achieved excellent results [29]. Li et al. developed an advance abutment pressure distribution model to study the distribution law of mining-induced stress under hard roof conditions and proposed a novel method of reckoning intensive factors by monitoring the support pressure [30]. Liu et al. developed a novel method involving hydraulic fracturing to generate vertical cracks to cut off a hard hanging-roof to control the deformation induced by mining the surrounding rock in roadway 5103 of Datong coal mine in China [31]. Zhao et al. first developed a multifield coupling model to investigate the distribution and evolution of stress, permeability, and gas flow field in the conventional and hard roof stopes after the protective seam mining [32]. Sun et al. developed a KZ54-type cutting bit to cut transverse grooves in the hard immediate roof and used directional hydraulic fracturing technology (DHFT) to control roof fracturing and collapse [33].

In summary, the roof control methods mainly include underground support, roof cutting, filling mining, presplitting blasting, and borehole pressure relief, but all have limitations in controlling high-position THR. Yu et al. proposed ground fracturing technology and achieved certain results in Datong Coal Mine [34–36]. Lu et al. used the secondary developed FLAC3D simulation software to determine the target layer of surface fracturing [37]. Gao et al. used the physical model and ABAQUS to research the characteristics of the overburden displacement and strata breaking strength after the vertical crack and horizontal crack existed in the high-level hard roof [38–40]. Based on the self-bearing of bulking rocks, the stability principle of the surrounding rock, and energy dissipation theories, Pan et al. obtained the criteria for determining the fracturing horizon and thickness of the HHR [41]. However, the above studies did not consider the influence of different fracturing positions on the fracture characteristics of high-position THR.

This study theoretically analyzed the mechanism of ground fracturing controlling mine earthquake induced by THR fracture first. Then, taking the $63_{up}06$ working face as the background, the FLAC numerical model was built to study the deformation and fracture law of high-position THR, the evolution laws of formation stress, and displacement under different fracturing positions. The fracturing test was carried out in the $63_{up}06$ working face, and the large-energy mine earthquake events decreased significantly after fracturing. The research results can provide some theoretical and practical guidance for mine earthquake control in working faces with similar geological conditions like Dongtan coal mine.

2. Engineering Background

2.1. Overview of Coal Mine. Dongtan coal mine is located in the border of the three cities of Zoucheng, Yanzhou, and Qufu in Shandong Province, China. As shown in Figure 1, the no. 6 mining district is located in the south wing of Dongtan minefield, the northern boundary is the security coal pillar of the industrial square, the southern boundary is adjacent to Nantun coal mine, the western boundary is adjacent to the no. 4 mining district, and the eastern boundary is the Yishan fault coal pillar. The no. 6 mining district is about 3.4 km long from east to west and 1.8~2.8 km wide from north to south and covers an area of about 6.9 km^2, the ground elevation is +43.52~+55.51 m with an average of +48.43 m, and the underground elevation is -650 m~-750 m. The $63_{up}06$ working face is located in the north of the no. 6 mining district, the goaf of 63up05 in the north, and the panel $63_{up}07$ (not developed) in the south. The strike length of the 63up06 working face is 1456.3 m, the dip width is 261.0 m, the total area of the working face is 379661.0 m^2, and the recoverable reserves are $2.474e^8$ kg. The lithology of strata above the coal seam is shown in Table 1.

2.2. Statistics of Mine Earthquake Events. The $63_{up}04$, $63_{up}05$, and $63_{up}03$ working faces in the mining district have been completed. During the mining period, the mine earthquake events occurred frequently in the mining district. The statistics of high-energy mine earthquake events (magnitude > 2.0) occurring 500 m before mining in three panels are carried out, as shown in Figure 2; the number of high-energy mine earthquake events in $63_{up}04$, $63_{up}05$, and $63_{up}03$ working faces is 23, 36, and 16, respectively, and all the large-energy mine earthquake events occurred 100 m~00 m above the goaf behind the working face. As shown in Table 1, there is 263.4 m sandstone stratum group about 100 m above the coal seam. Therefore, it is preliminarily concluded that the occurrence of high-energy mine earthquake events may be related to the fracture of the thick and hard sandstone above the coal seam. The collapse step of this part of the rock stratum is large, and enormous elastic deformation energy is released during strata fracture, which causes the vibration of the rock stratum and further leads to the occurrence of high-energy mine earthquake events.

Table 1: Lithology of overlying strata above the coal seam (O2-D7 drilling data).

No.	Bottom depth (m)	Thickness (m)	Lithology
1	125.85	125.85	Cap rock
2	315.05	189.2	Sandstone group
3	316.55	1.5	Mudstone
4	324.7	8.15	Sandstone
5	326	1.3	Sandy mudstone
6	589.4	263.4	Sandstone group
7	602	12.6	Sandy mudstone
8	603.25	1.25	Sandstone
9	604.2	0.95	Mudstone
10	605.1	0.9	Sandstone
11	609.5	4.4	Mudstone
12	619.4	9.9	Sandstone
13	628.4	9	Sandy mudstone
14	630.45	2.05	Mudstone
15	632.85	2.4	Sandstone
16	635.7	2.85	Sandy mudstone
17	643.7	8	Sandstone
18	652.4	8.7	Sandy mudstone
19	654.15	1.75	Medium sandstone
20	659.35	5.2	Fine sandstone
21	662.6	3.25	Mudstone
22	664.3	1.7	2 coal
23	665.9	1.6	Mudstone
24	669.83	3.93	Fine sandstone
25	670.58	0.75	Medium sandstone
26	673.08	2.5	Fine sandstone
27	673.58	0.5	Medium sandstone
28	675.53	1.95	Fine sandstone
29	680.95	5.42	3_{up} coal
30	692.43	11.48	Siltstone

2.3. Occurrence Mechanism of Mine Earthquake. As shown in Figure 3, the hanging length of the THR gradually increases with the advance of the working face; a large quantity of elastic energy is stored in the THR before breaking. When the bending tensile stress of the THR reaches the tensile strength, the THR will break, and the gravitational potential energy and elastic energy released by breakage will be transformed into impact kinetic energy, which will work on the lower rock stratum to produce impact vibration wave. The impact vibration wave will cause the disturbance of rock mass in the process of propagation in the rock stratum and then induce dynamic response phenomena such as mine earthquake. The relationship of the THR hanging length and the mining length of the coal seam is shown in Figure 4.

$$l = l_0 - 2h_L \cot \alpha, \quad (1)$$

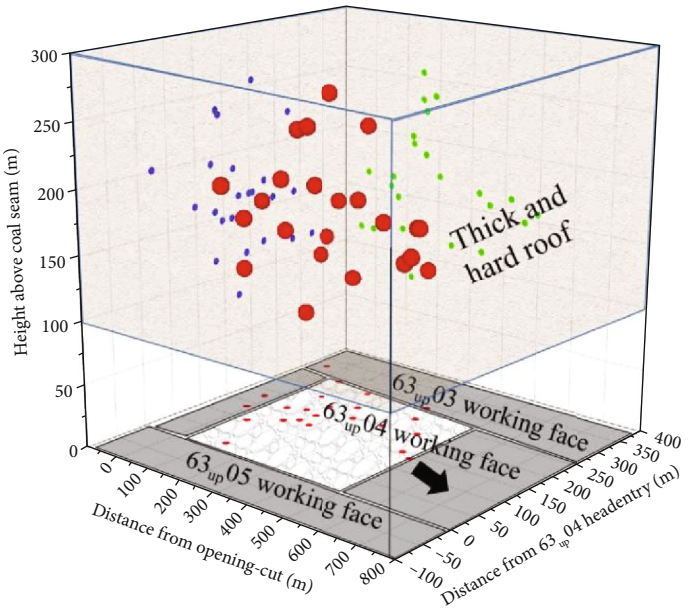

(a) $63_{up}04$ working face

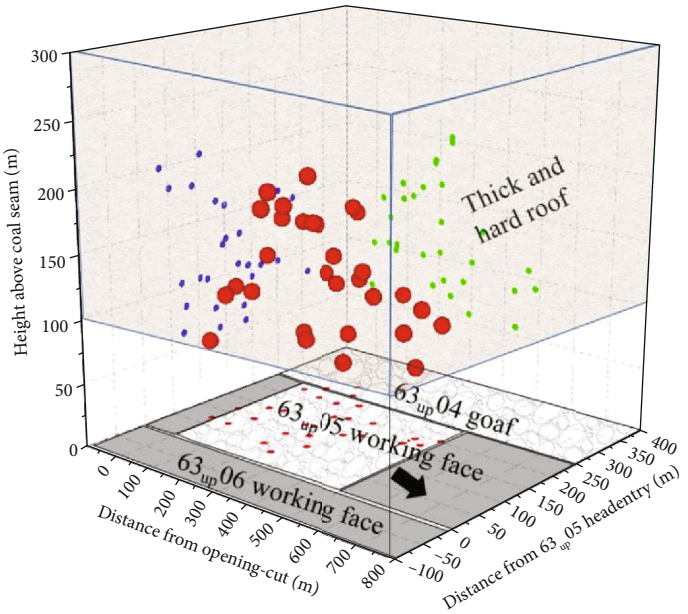

(b) $63_{up}05$ working face

Figure 2: Continued.

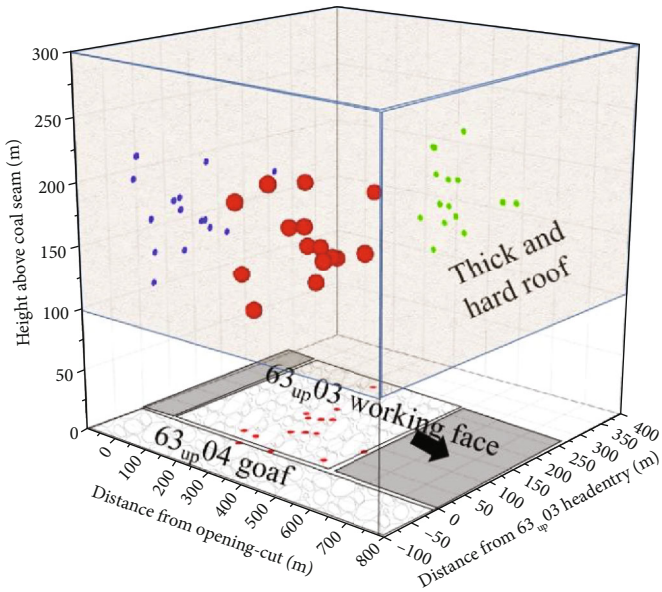

(c) $63_{up}03$ working face

Figure 2: Occurrence times of high-energy mine earthquake events in the no. 6 mining district.

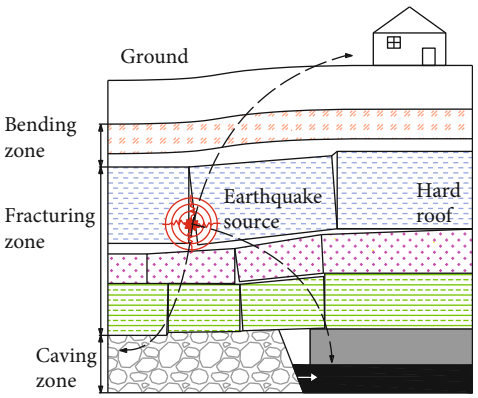

Figure 3: Schematic diagram of the mine earthquake induced by THR fracture.

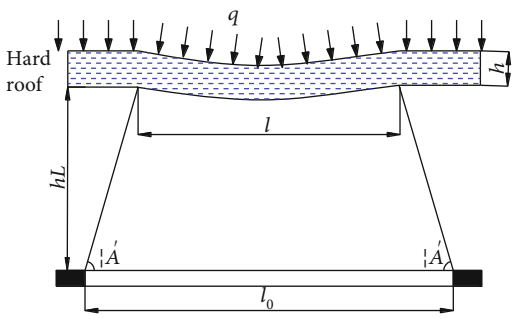

Figure 4: Relationship between the hanging length and mining length.

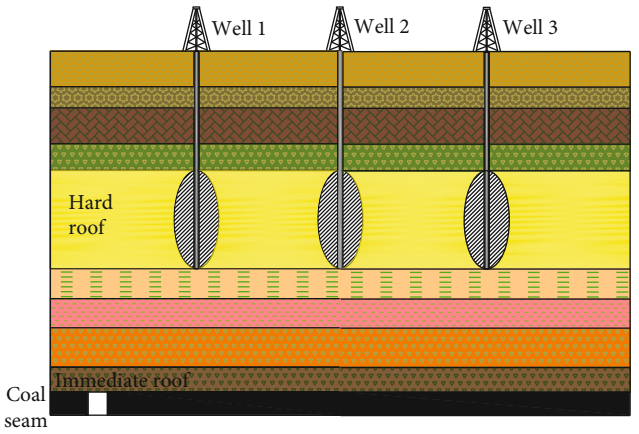

Figure 5: Schematic of the ground fracturing technology.

where l is the THR hanging length (m), l_0 is the mining length (m), h_L is the vertical distance above the coal seam (m), and α is the breaking angle (°).

According to the law of energy conservation, the energy released by the THR breakage mainly includes the gravitational potential energy, the elastic deformation energy, and the kinetic energy [42].

$$U = U_G + U_E + U_K, \tag{2}$$

where U is the total energy released (J), U_G is the gravitational potential energy (J), U_E is the elastic deformation energy (J), and U_K is the kinetic energy (J).

$$U_G = mgH, \tag{3}$$

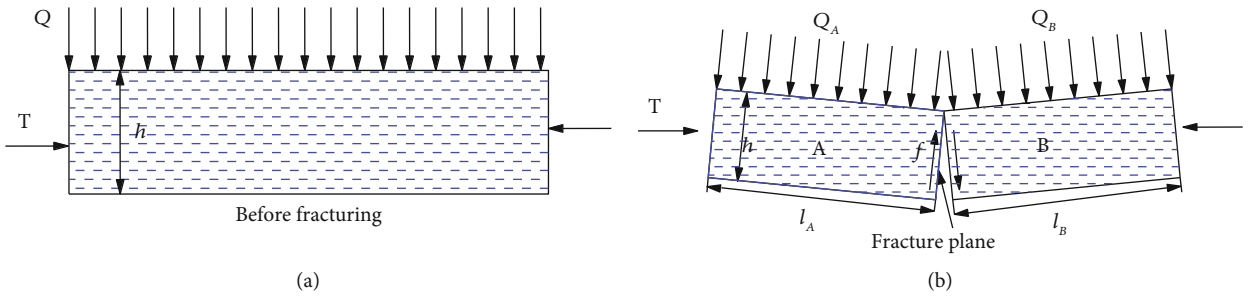

Figure 6: The stress analysis of cutting block in fracturing horizon: (a) before fracturing and (b) after fracturing.

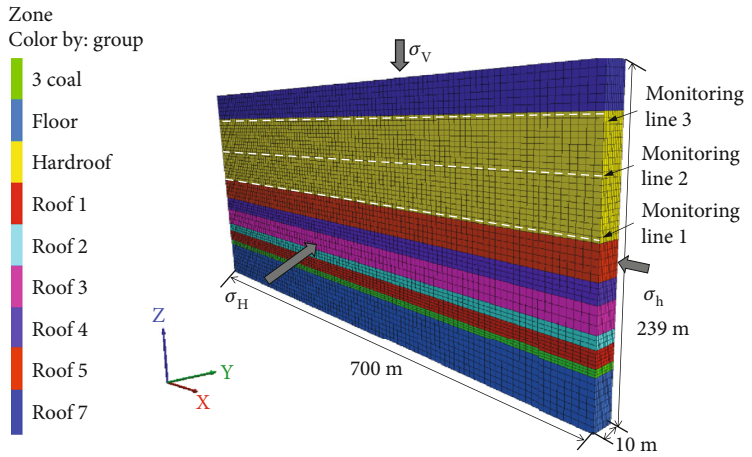

Figure 7: The numerical simulation model.

Table 2: Rock mass physical and mechanical properties.

Name	Lithology	Depth (m)	Thickness (m)	Bulk modulus (GPa)	Shear modulus (GPa)	Cohesion (MPa)	Internal friction angle (°)	Tensile strength (MPa)	Density (kg/m^3)
Roof7	Mudstone	360	30	5.6	4.1	3.0	38	1.2	2350
Hard roof	Fine sandstone	390	100	24.7	19.1	5.3	48	6	2700
Roof5	Mudstone	490	30	5.6	4.1	3.0	38	1.2	2350
Roof4	Sandy mudstone	520	18	8.3	6.5	5.3	45	1.5	2500
Roof3	Siltstone	538	25	5.8	4.4	3.2	30	2.08	2430
Roof2	Mudstone	563	15	5.6	4.1	3.0	38	1.2	2350
Roof1	Sandy mudstone	578	16	8.3	6.5	5.3	45	1.5	2500
Coal seam	Coal	594	6	3.8	2.6	5	32	0.5	1450
Floor	Siltstone	600	40	5.8	4.4	3.2	30	2.08	2430

$$U_E = \frac{q^2 l^5 l_0}{48Eh^3}, \tag{4}$$

$$U_K = \frac{1}{2} m \left(\frac{du}{dt}\right)^2, \tag{5}$$

where H is the lower separation space height (m), m is the total mass of broken strata (kg), q is the average load of the upper rock stratum (Pa), E is the elastic modulus (Pa), h is the thickness of the THR (m), and u is the displacement of THR (m).

Then, the following can be obtained when formulas (3), (4), and (5) are substituted into

$$U = mgH + \frac{q^2 l^5 l_0}{48Eh^3} + \frac{1}{2} m \left(\frac{du}{dt}\right)^2. \tag{6}$$

Table 3: Physical and mechanical parameters of interface element.

Name	Normal stiffness (GPa)	Tangential stiffness (GPa)	Cohesion (MPa)	Internal friction angle (°)	Tensile strength (MPa)
Hydraulic fracture	3	3	—	20	—

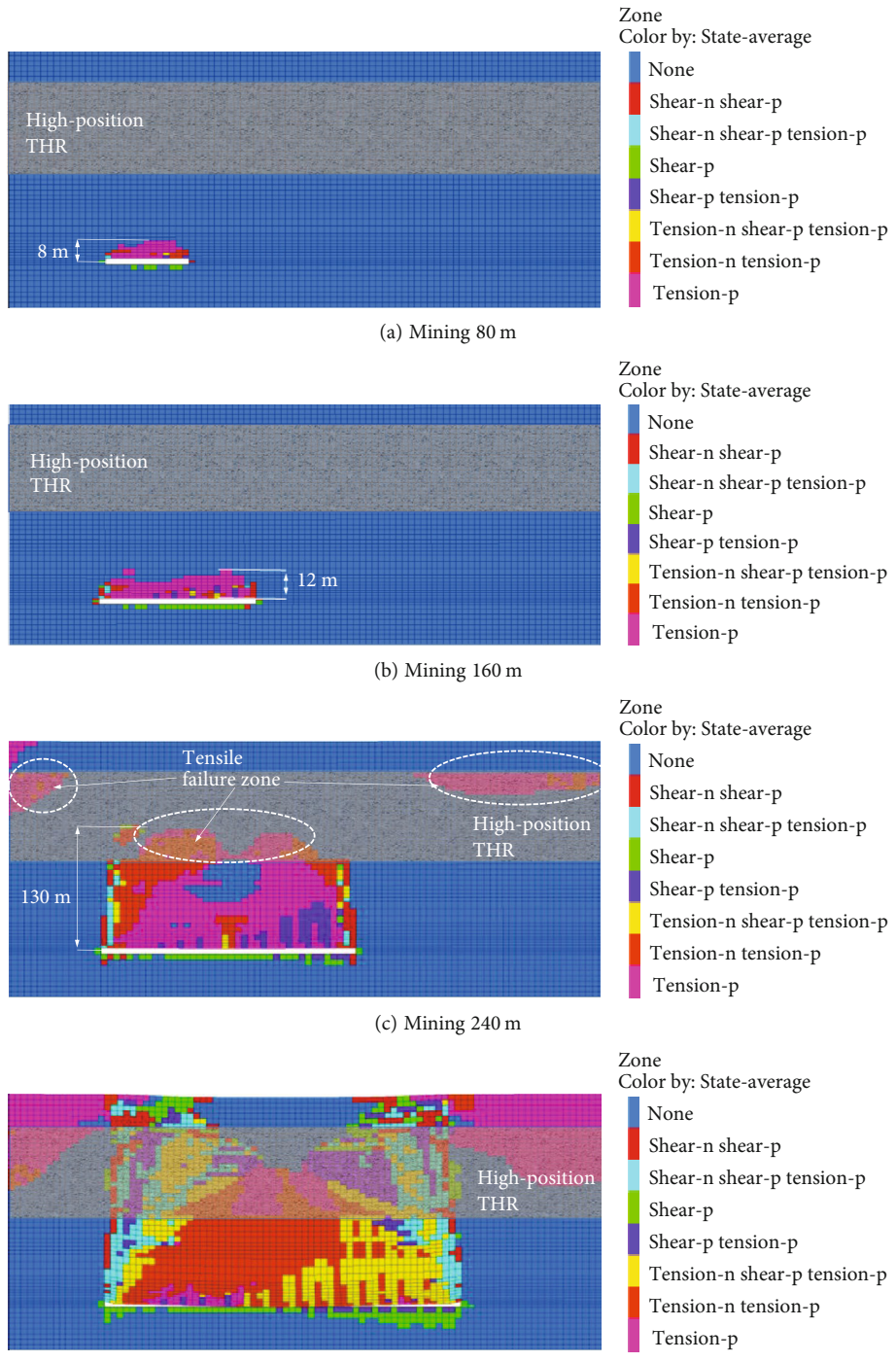

Figure 8: Plastic zone change during excavation.

According to the above formula, it can be found that the energy released by the THR breakage is mainly related to the THR hanging length, upper load, and THR movement velocity. In general, most of the elastic energy is released in the form of thermal energy and acoustic emission, and the seismic efficiency (the ratio of seismic energy to elastic energy released in the fracture process) Ω is only 0.26%~3.6%. At the same time, due to the layered and heterogeneous characteristics of the stratum, the energy attenuation of seismic wave in the stratum medium is a power exponential attenuation function of the propagation path distance, which is approximately expressed as follows:

$$U' = \Omega U r^{-\lambda}, \tag{7}$$

where U' is the energy after a certain distance of seismic wave propagation (J), r is the spatial distance of seismic wave propagation (m), and λ is the attenuation constant related to formation medium.

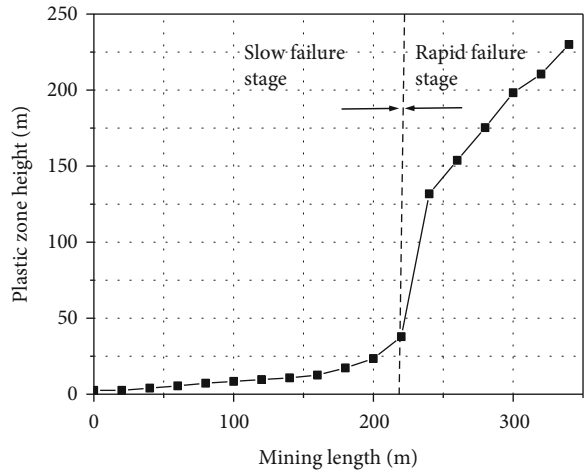

Figure 9: The maximum height change of the plastic zone.

2.4. The Mechanism of Controlling Mine Earthquake by Ground Fracturing. Dongtan coal mine is preparing to mine the $63_{up}06$ working face. In order to ensure the safe and efficient production of coal mining, it is proposed to conduct ground fracturing experiment before mining to cut off the high-level hard and thick roof to reduce the roof breaking span and weaken the rock strength, as shown in Figure 5, so as to avoid the occurrence of large-energy mine earthquake events caused by the hard roof fracture.

When the vertical fracture occurs in the fractured layer, the stress state of the rock stratum changes [43–45]. The two ends of the stratum are in the state of fixed support stress, and the stratum is cut into blocks A and B by the fracture plane, which is similar to the hinged structure. The stress analysis of the hard roof after fracturing is shown in Figure 6.

$$T \tan \beta = f, \tag{8}$$

$$f \le |(Q_A + G_A) - (Q_B + G_B)| \tag{9}$$

where T is the horizontal thrust on both sides of the rock stratum (kN), f is the friction force on the fracture surface of the rock block during rotation (kN), β is the internal friction angle (°), Q_A and Q_B are the gravity of the overlying rock stratum (kN), and G_A and G_B are the gravity of the rock stratum itself (kN).

Under the influence of the overlying rock stratum and self-weight, stress concentration is easy to occur around the fracture surface after fracturing in the formation, which will cause damage to the rock mass around the fracture surface and weaken the horizontal force between blocks A and B. The friction force on the fracture surface is not enough to maintain the balance between the cutting blocks. The cutting blocks will shear and slip, and the pressure will be released in advance. At the same time, the blocks on both sides of the fracture surface are more likely to break and rotate under the action of vertical force, causing A and B to break at the fixed support ends on both sides, causing the instability of the rock stratum. And the fracturing fluid is retained in the formation, which plays a certain role in hydration of the rock and weakens the strength of the rock. Therefore, under the condition of occurrence of vertical fracture plane, the stress state and occurrence form of rock stratum change, the rock stratum is more likely to rotate along the fracture surface under the action of vertical force, the breaking span of the rock stratum is reduced, and the breaking instability strength will be weakened, which can effectively reduce the energy release and grade of mine earthquake induced by the THR breakage.

3. Numerical Simulation

3.1. Numerical Model. In order to further study the strata fracture characteristics in the presence of high-position THR before and after fracturing, as shown in Figure 7, a simplified strata model was established by using FLAC3D. The model size is 700 m × 10 m × 239 m (length × width × height), and it consists of 57000 zones and 64438 grid points. The thickness of the coal seam is 6 m, which is simplified as a horizontal coal seam. The thickness of THR is 100 m, which is 100 m away from coal seam in the vertical direction. In addition, three monitoring lines were arranged at the top, middle, and lower part of the THR to monitor the displacement and stress changes during excavation. The physical and mechanical parameters of each stratum are shown in Table 2.

The upper boundary of the model is a free boundary, and the vertical stress is applied to simulate the gravity of 360 m overlying strata. In the bottom boundary, the vertical and horizontal displacements are fixed. In the two lateral boundaries, horizontal displacement is constrained. Considering that the excavated stratum can be simplified into a plane strain model, the displacement along the y-axis direction is fixed. The 100 m coal pillars are reserved on both sides to eliminate the boundary effect. The mining length of the working face is 500 m. The mining method is strike longwall mining, and the natural caving method is used to manage the roof. According to the in situ stress data, the initial in situ stress field is inversed; when the model reaches

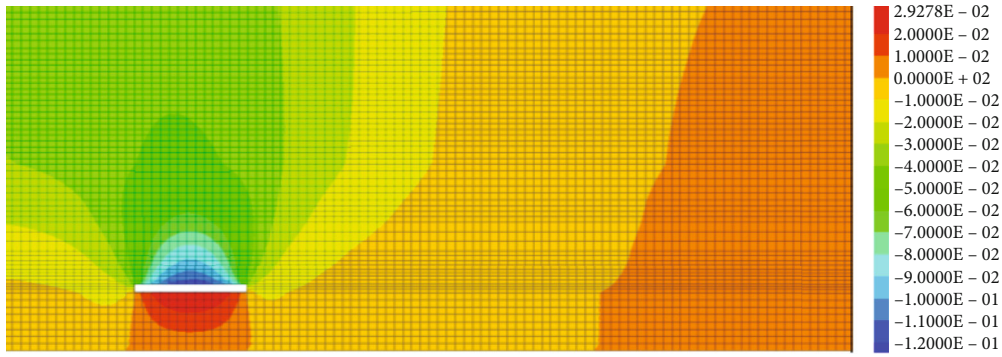

(a) Mining 80 m

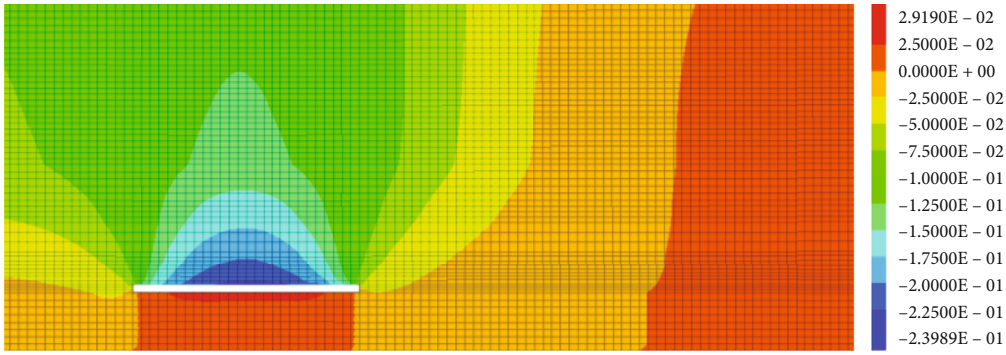

(b) Mining 160 m

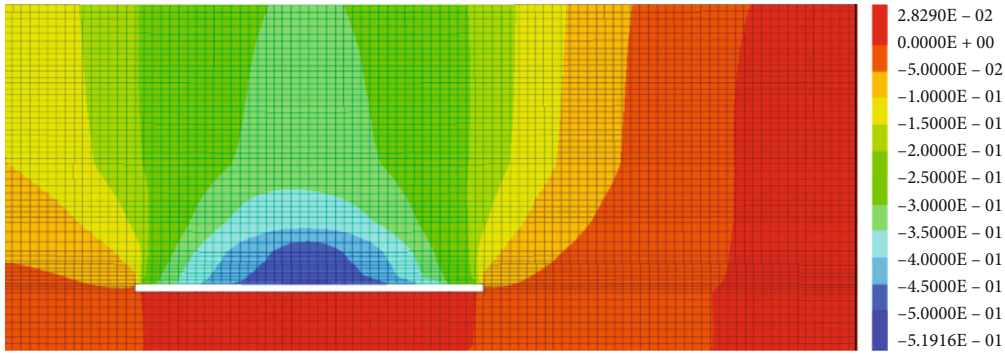

(c) Mining 240 m

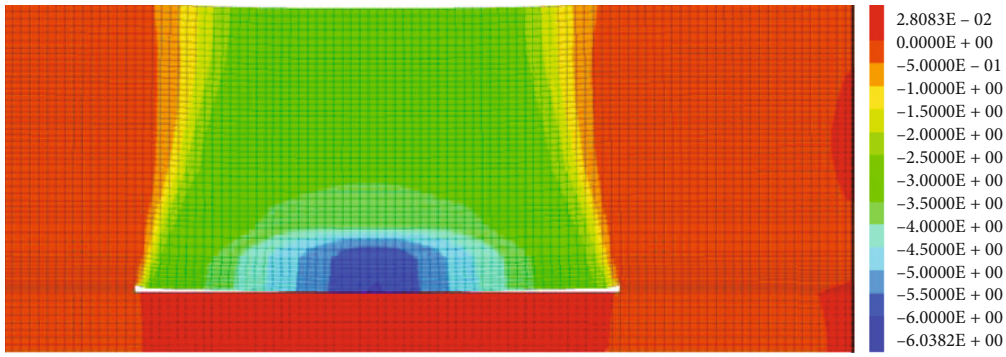

(d) Mining 340 m

Figure 10: The vertical displacement nephograms during excavation.

the initial equilibrium, the stress in the coal seam is $\sigma_h = -11.54$ MPa, $\sigma_H = -25.3$ MPa, and $\sigma_V = -16.75$ MPa, which reflects the real situation of the strata.

3.2. Simulation Scheme Design. In this simulation, it is planned to first study the fracture and collapse law of THR before fracturing during coal seam excavation and then

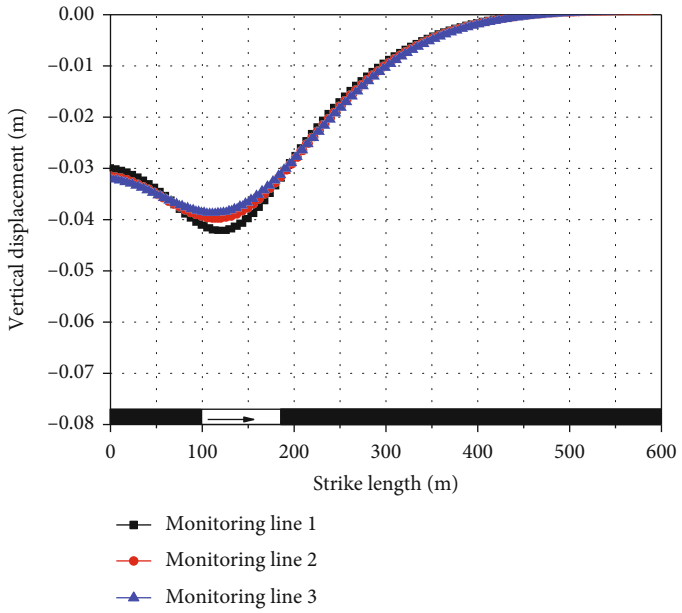

(a) Mining 80 m

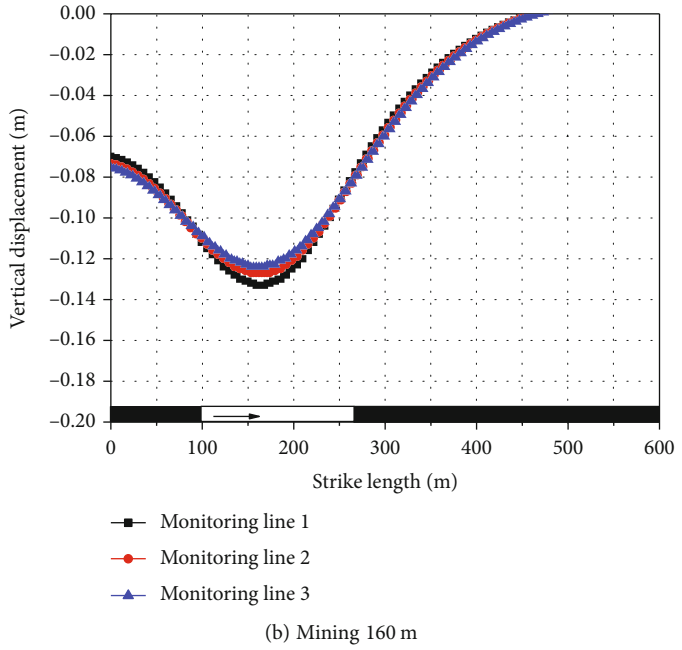

(b) Mining 160 m

Figure 11: Continued.

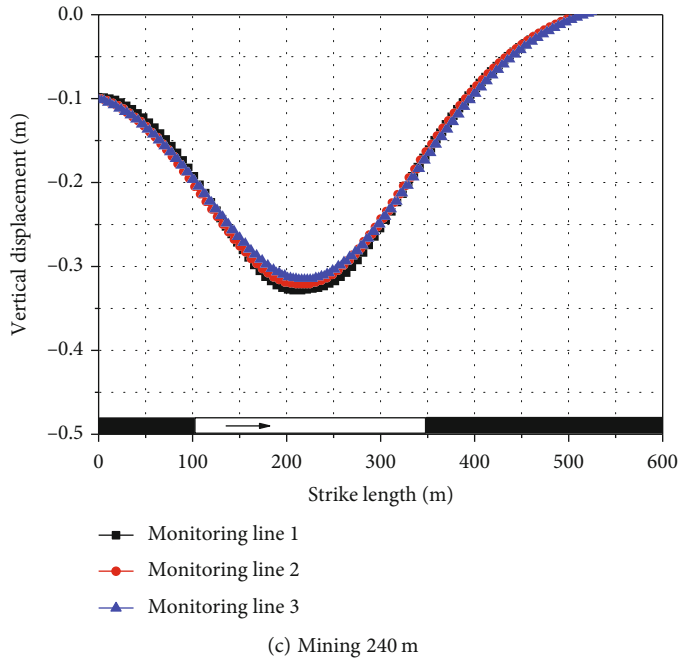

(c) Mining 240 m

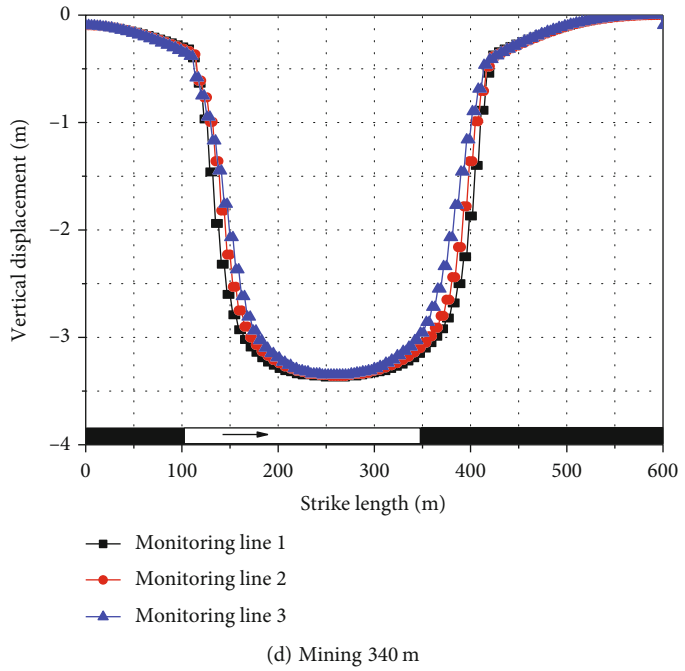

(d) Mining 340 m

Figure 11: The subsidence curve at different positions of THR during the mining process.

study the impact of single hydraulic fracture at different positions on the rock stratum fracture. The hydraulic fracture is a vertical fracture, the fracture runs through the whole high-position THR, and the fracturing position is located 0 m, 50 m, 100 m, 150 m, 200 m, and 250 m in front of the opening cut; the interface element in FLAC software is used to simulate hydraulic fractures, and the element has friction angle, cohesion, expansion angle, normal stiffness, tangential stiffness, tensile and shear bond strength, and other parameters, which can well simulate the process of sliding, opening, and complete breaking between crack surfaces. And the mechanical parameters at the interface element in this paper are shown in Table 3 [46, 47].

4. Simulation Results

4.1. Movement Law of High-Position THR before Fracturing

4.1.1. Plastic Zone Change. The distribution of the plastic zone can directly reflect the fracture of the upper rock stratum after coal seam excavation. The Mohr-Coulomb constitutive model adopted in this paper is an ideal elastoplastic

constitutive model. When the element stress exceeds the yield strength, plastic deformation will occur. After reaching the yield stress, there are two failure modes, tensile failure (tension-*n*) and shear failure (shear-*n*). However, when the stress state of the rock mass changes less than the yield stress, the previous plastic deformation is retained; that is, the area is judged as the previous shear failure (shear-*p*) and previous tension failure (tension-*p*). Figure 8 is the plastic zone distribution map under different mining lengths. Figure 9 is the strata failure height evolution law curve. It can be seen from Figure 8 that the strata above the goaf began to destroy after mining and presented a typical "hump shape" failure mode. The failure mode above the goaf was mainly tensile failure. The stress concentration on both sides of the goaf was obvious, and tensile and shear failure occurred in this area. When the coal seam was mined to 80 m, the failure height reached 8 m and the failure range was small; when the coal seam was mined to 160 m, the failure height increased slightly to 12 m; meanwhile, the high-position THR had not been damaged because of its large thickness and high strength; when the coal seam was mined to 240 m, the failure height reached 130 m, the bottom of the THR was damaged, and a small amount of tensile failure was generated on both sides of the THR top area. Then, the THR failure height increased, and a large number of tensile shear failure areas were generated on both sides of the THR. Until the mining distance reached 340 m, the strata failure height runs through the whole THR. It can be concluded that the THR breaking span is 340 m.

As can be seen from Figure 9, the strata fracture during excavation can be roughly divided into two stages with the mining distance of 220 m as the boundary: the slow failure stage before 220 m and the rapid failure stage after 220 m. The growth rate of strata fracture height before mining 220 m was relatively slow, and the maximum failure height only reached 38 m. After mining 220 m, the growth rate of strata failure height had increased significantly. This is because in the early stage, there was the support of high-position THR, the upward propagation speed of strata failure was relatively slow, and the failure developed to the bottom and both sides of the top of the THR in the later stage; in addition, the bearing capacity decreased gradually, so the development of fracture height entered a rapid stage.

4.1.2. Vertical Displacement Change. Figure 10 shows the vertical displacement nephograms under different mining lengths, and Figure 11 is the subsidence curve at different positions of THR. It can be seen from Figure 10 that after mining, the roof above the goaf began to sink, and the maximum subsidence position occurred at the center of the roof above the goaf. With the increase in excavation length, the vertical displacement continued to increase. When the coal seam was excavated to 80 m, the maximum subsidence value reached 0.12 m, and the subsidence was small; when the coal seam was excavated to 160 m, the maximum subsidence value reached nearly 0.24 m, and the growth rate was still slow, only 0.12 m higher than that when the coal seam was excavated to 80 m; when the excavation reached 240 m, the maximum subsidence value reached 0.52 m, and the subsidence value at the bottom of the high-position THR increased. When the coal seam was excavated to 340 m, the maximum subsidence value reached 6.03 m, the calculation was no longer convergent, and the THR reached the first breaking span.

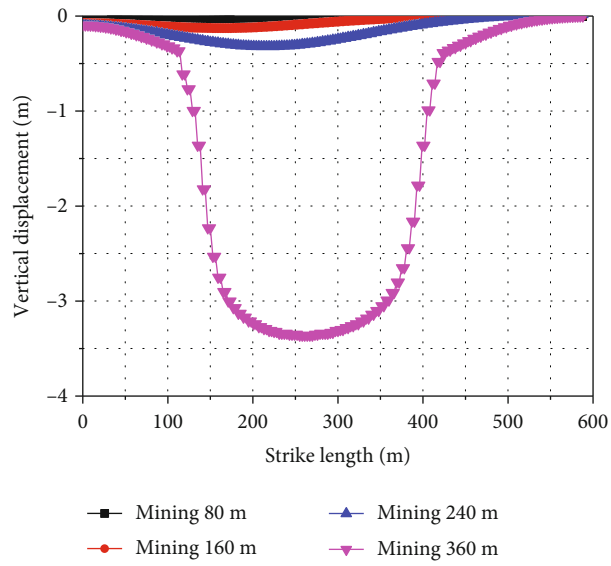

Figure 12: The vertical displacement in the THR middle part under different mining distances.

As shown in Figure 11, in the first 240 m of excavation, the subsidence rate of the THR bottom part preceded the middle and upper part. The subsidence of the rock stratum near the opening cut was higher than that far away from the opening cut; with the increase in the excavation length, the subsidence value of the upper rock stratum was gradually close to that of the lower rock stratum. When the THR reached the first breaking span, the subsidence curves of the upper and lower part near the maximum subsidence position almost overlap. Figure 12 displays the vertical displacement in the THR middle part under different mining distances. It can be seen that when the THR reached the first breaking span, the THR subsidence peak value reached 3.4 m, and the subsidence increased sharply, which once again showed the integrity and instantaneity of high-position THR when it breaks.

4.1.3. Horizontal Stress Change. During the mining process, the deformation and failure of the strata are related to the rock stress state. Therefore, the horizontal stress distribution of the strata under different excavation distances and the horizontal stress distribution at different positions of the THR were selected for analysis. Figure 13 displays the whole strata horizontal stress nephogram during excavation, and Figure 14 is the horizontal stress variation curve at different positions of THR. As can be seen from Figure 13, after mining, the horizontal stress above the goaf decreased and some tensile stress areas appeared, and the horizontal stress concentration occurred on both sides of the goaf, mainly compressive stress. When the coal seam was mined to 80 m, the maximum compressive stress appearing on the coal wall

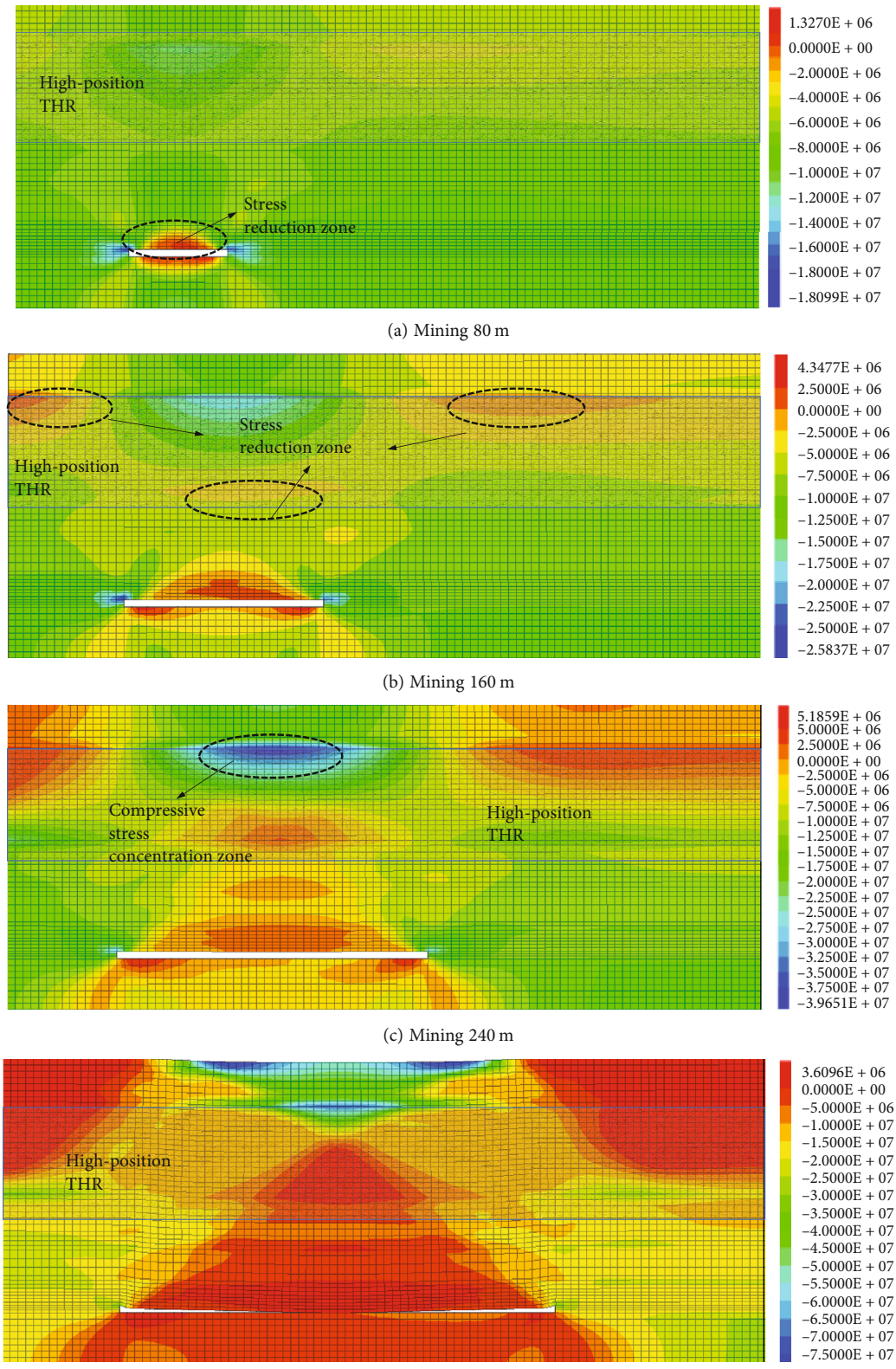

Figure 13: The horizontal stress distribution under different excavation distances.

on both sides of the goaf reached 18.1 MPa, and a little tensile stress concentration occurred within 20 m above the goaf; when the coal seam was mined to 160 m, the range of the reduction of horizontal compressive stress continued to increase, and the reduction of compressive stress at the THR bottom part and both sides of the THR top part is

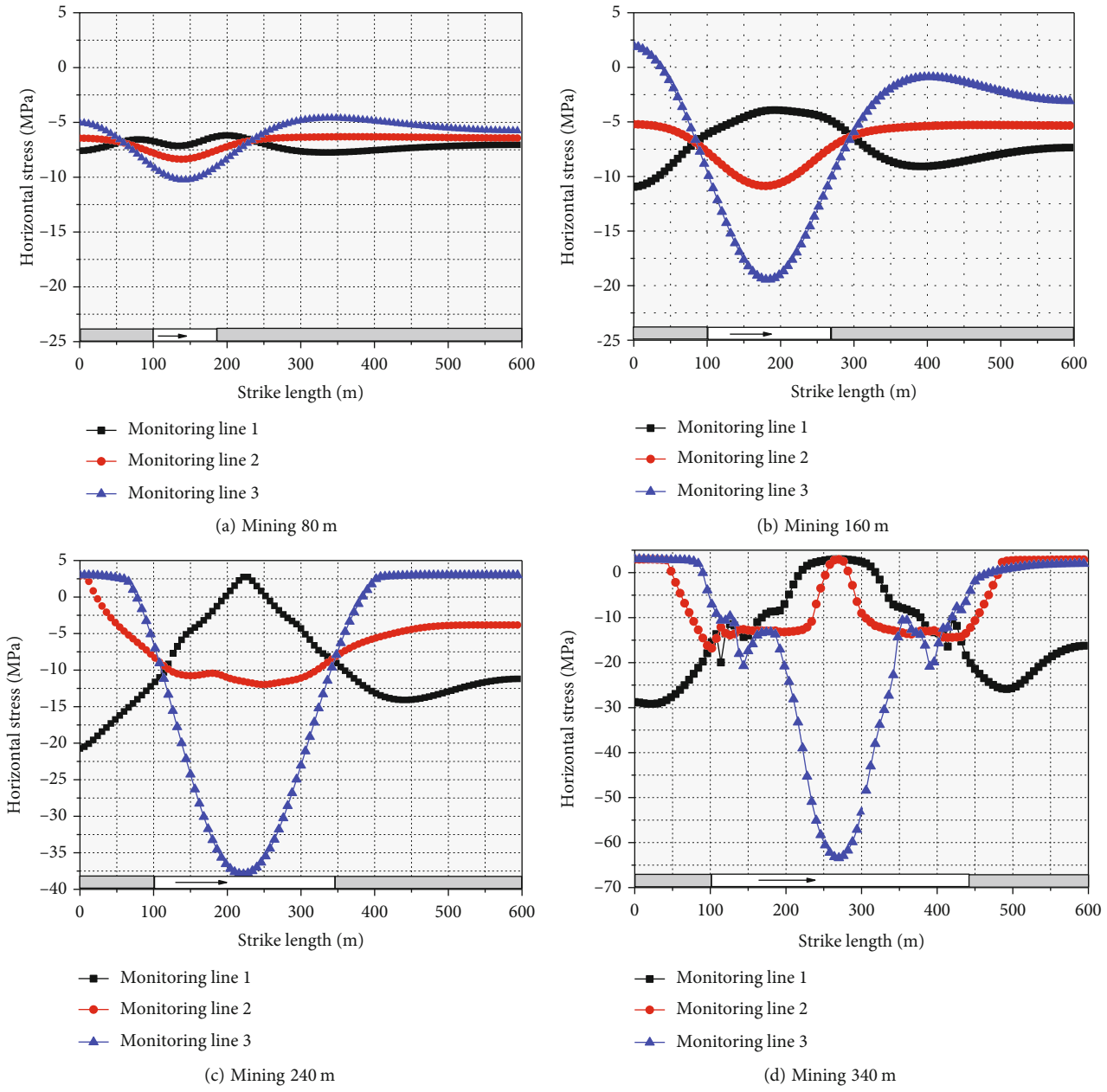

Figure 14: The horizontal stress variation curve at different positions of THR.

obvious; meanwhile, the coal seam excavation had disturbed the THR to a certain extent. When the coal seam was excavated to 240 m, the horizontal compressive stress continuously transferred to the upper part of the stratum, and the maximum compressive stress appearing in the center above the goaf, close to the center of the THR top part, reached 39.6 MPa, which is caused by the loss of stress support under the THR and bearing the weight of the overlying strata. When the coal seam was excavated to 340 m, the THR reached the first breaking span, and a wide range of horizontal tensile stress areas appeared on both sides of the bottom and top of the THR.

It can be seen from Figure 14 that when the coal seam was excavated to 80 m, the horizontal stress decreased slightly at the THR bottom part, and the horizontal compressive stress increased slightly at the middle and top of the THR. When the coal seam was excavated to 160 m, the above situation became more obvious. When the coal seam was excavated to 240 m, the horizontal tensile stress appeared at the THR bottom part and both sides of the top part, which is caused by the fracture and continuous bending and subsidence at the THR bottom part. When the coal seam was excavated to 340 m, the horizontal compressive stress was further transferred upward, and part of the tensile stress also appeared in the middle of the THR. From the above analysis, it can be seen that the high-position THR fracture caused by coal seam excavation was related to the continuous upward transfer of horizontal compressive stress, resulting in the concentration of horizontal compressive stress in THR. Therefore, overcoming

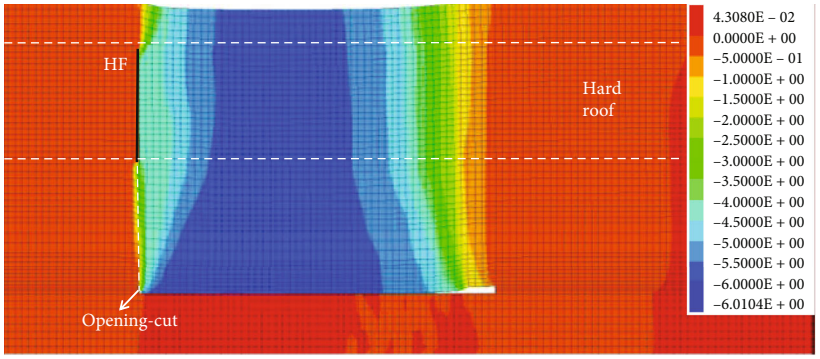

(a) 0 m away from the opening cut

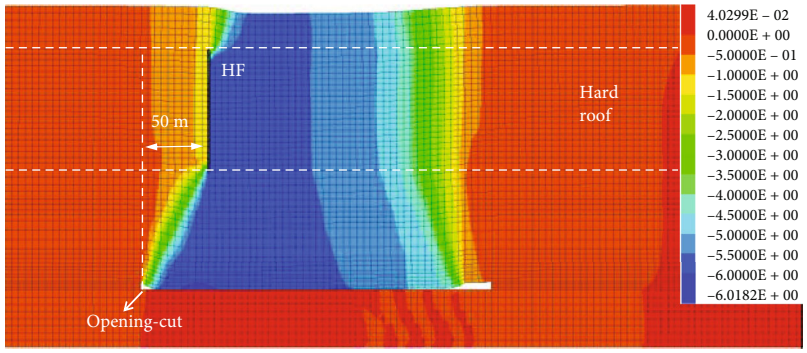

(b) 50 m away from the opening cut

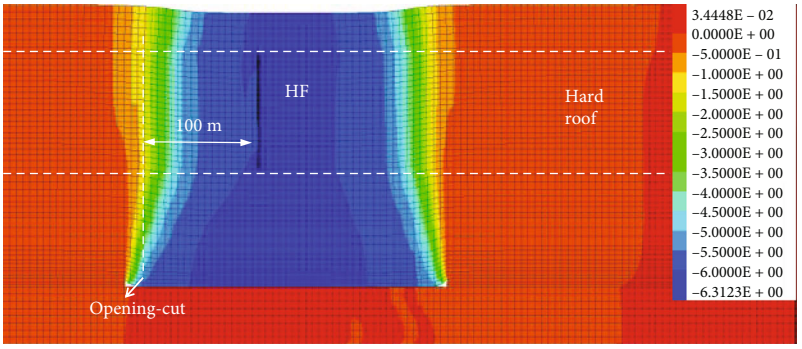

(c) 100 m away from the opening cut

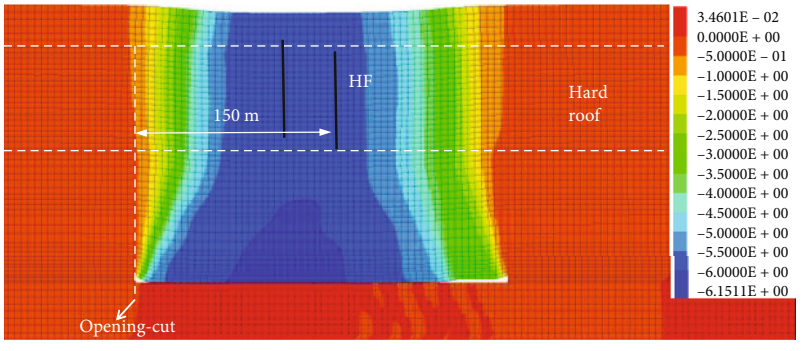

(d) 150 m away from the opening cut

Figure 15: Continued.

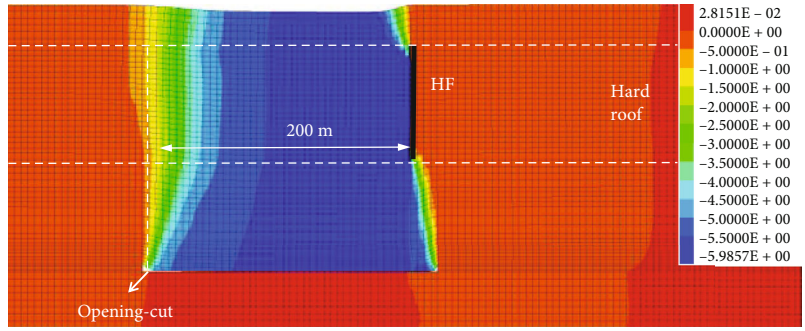

(e) 200 m away from the opening cut

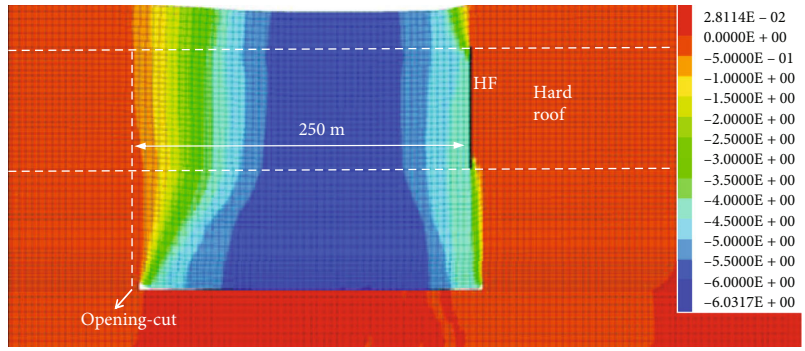

(f) 250 m away from the opening cut

Figure 15: The vertical displacement nephogram when the THR reaches the first breaking span under different fracturing positions.

the concentration of horizontal compressive stress can effectively alleviate the dynamic disaster caused by the large-area overall fracture of high-position THR.

4.2. The THR Movement Laws after Fracturing

4.2.1. Vertical Displacement. Figure 15 displays the vertical displacement nephogram when the THR reaches the first breaking span under different fracturing positions, and Figure 16 shows the subsidence curve in the THR middle part under different fracturing positions. It can be seen from Figure 16 that after fracturing, the whole strata had a more sufficient falling degree after excavation than before fracturing, the THR had obvious sliding deformation at the hydraulic fractures, and the first breaking span in all fracturing schemes was reduced as shown in Table 4. It can be concluded that the THR first breaking span is roughly similar under different fracturing schemes, which was greatly reduced compared with that without fracturing, the high-position THR sinks synchronously with the lower weak rock stratum in the process of strata collapse, and there is no long-term roof hanging phenomenon in the process of excavation, so as to avoid the overall instantaneous fracture of the rock stratum, effectively reducing the release of energy.

The selection of different fracturing positions will have an impact on the THR fracture form. Therefore, the vertical displacement in the THR middle part under different fracturing schemes was selected for analysis. As shown in Figure 16, under different fracturing schemes, the THR maximum subsidence values were all close to 6 m, and there were obvious differences on both sides of the hydraulic fracture. When the fracture position was above the opening cut, the maximum subsidence value appeared at 55 m in front of the opening cut. The whole strata broke in the form of cantilever beam, and the overall range of fracture was large. When the fracture position was located 50 m in front of the opening cut, the maximum subsidence value occurred at the fracture position. There was a 50 m cantilever beam on the left side of the fracture. The subsidence value of this part of the rock stratum was small, and there will be a risk of breaking the hanging roof for a long time, which will become a potential safety hazard of dynamic disaster. The strata on the right side of the fracture broke integrally to one side of the goaf in the form of cantilever beam. When the fracture was located in 100 m and 150 m in front of the opening cut, the maximum subsidence value when the THR broke occurred near the hydraulic fracture, and the subsidence of the strata on both sides of the fracture presented an obvious symmetrical distribution form with the fracture as the center line; there was no overall cantilever breaking form, and the THR broke on both sides of the top and sank along the hydraulic crack in the middle. When the fracture was located in 200 m in front of the opening cut, the integral cantilever beam breaking form occurred on the left side of the fracture. When the fracture was located in 250 m in front of the opening cut, the THR maximum subsidence value appeared 100 m to the left of the fracture. To sum up, when the fracturing position is closed to the opening cut, the high-position THR presents an overall cantilever beam breaking form and deviates to one side of the goaf; the overall length of the cantilever beam is large, which may cause some potential safety hazards to the stope due to the

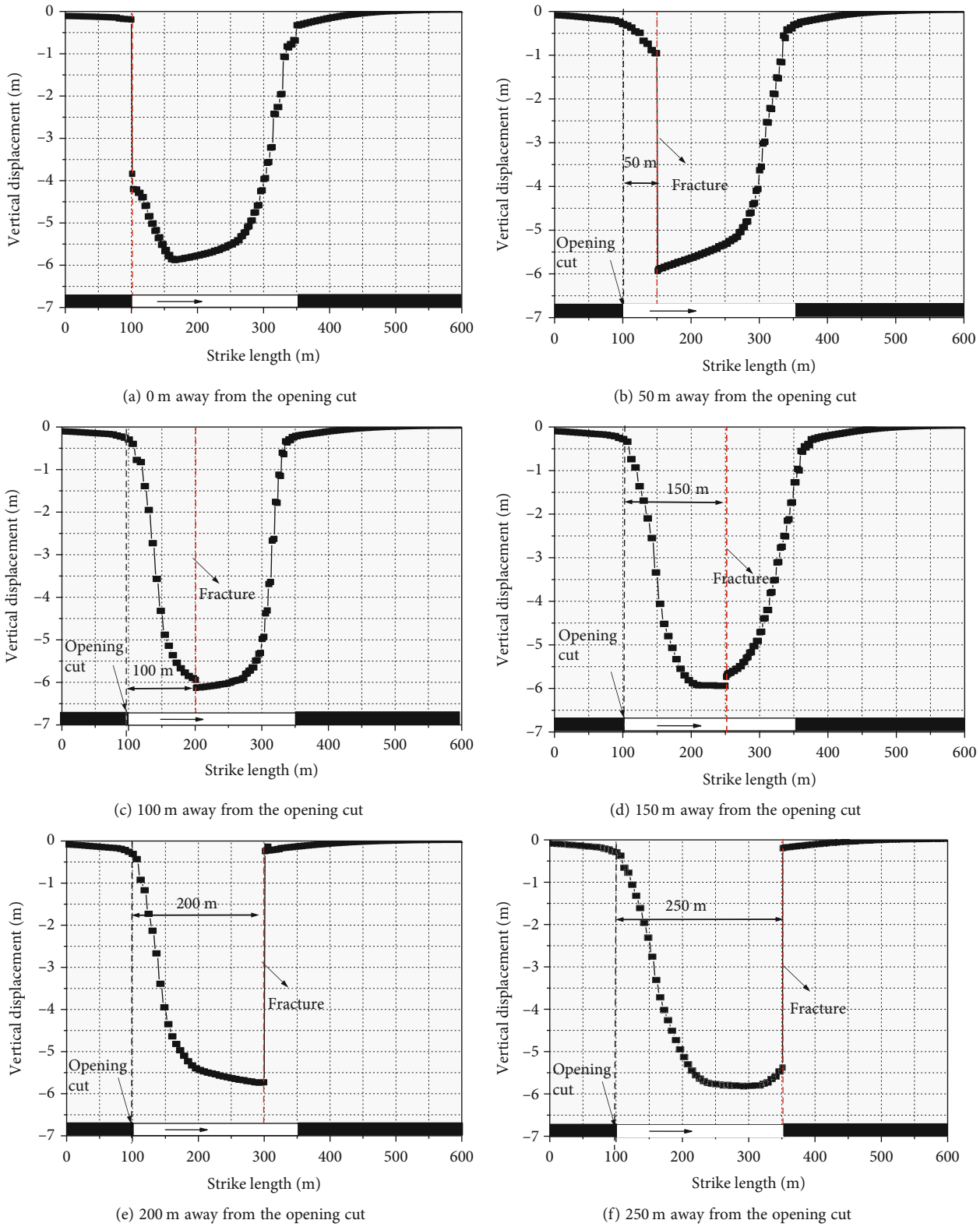

(a) 0 m away from the opening cut

(b) 50 m away from the opening cut

(c) 100 m away from the opening cut

(d) 150 m away from the opening cut

(e) 200 m away from the opening cut

(f) 250 m away from the opening cut

Figure 16: The vertical displacement curve at the THR middle part under different fracturing positions.

influence of the gravity of the rock stratum during breakage. When the fracturing position is close to the center of the first breaking span, there is no overall cantilever breaking form in the THR, the THR breaks on both sides of the top and sinks along the hydraulic fracture in the middle, and the collapse is relatively uniform.

Table 4: The first breaking span under different fracturing positions.

Fracturing position distance to the opening cut (m)	0	50	100	150	200	250
Breaking span (m)	240	260	280	240	260	240

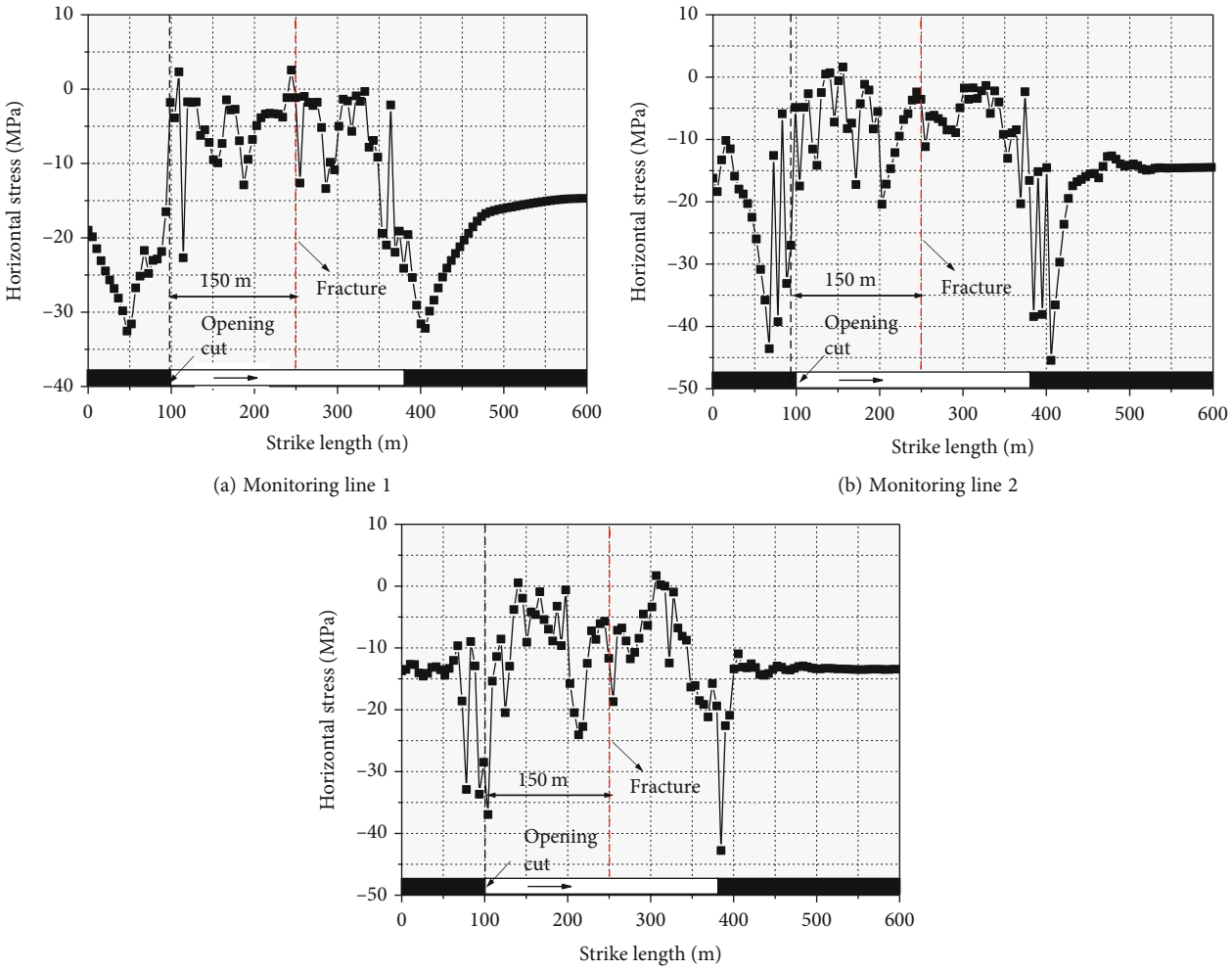

Figure 17: The horizontal stress change curve before the THR breaks (fracture position at 150 m away from the opening cut).

4.2.2. Horizontal Stress. Affected by the article length, this paper only selected the horizontal stress distribution of the THR when the fracture existed 150 m in front of the opening cut for analysis. It can be seen from Figure 17 that the horizontal stress distribution at different positions of the THR showed that the horizontal compressive stress above the goaf decreased, some tensile stress areas appeared, the compressive stress concentration appeared above the coal bodies on both sides, and the compressive stress at the lower part of the THR was significantly greater than that at the middle and upper part, which showed that when the hydraulic crack existed in the THR, the THR no longer bears the gravity of the overlying strata. During the excavation process, the horizontal compressive stress in the stratum does not transfer upward and concentrate. There is a large area of compressive stress reduction in the rock mass on both sides of the hydraulic fracture, so as to avoid the instantaneous release of energy when the THR breaks due to the high concentration of stress, which can play an effective role in the prevention and control of dynamic disasters.

5. Field Fracturing Test

Theoretical analysis and numerical simulation results have proven the feasibility of ground fracturing to control mine earthquake. The field fracturing test was carried out in the $63_{up}06$ working face in the no. 6 mining district of Dongtan coal mine. As shown in Figure 18(a), three fracturing wells

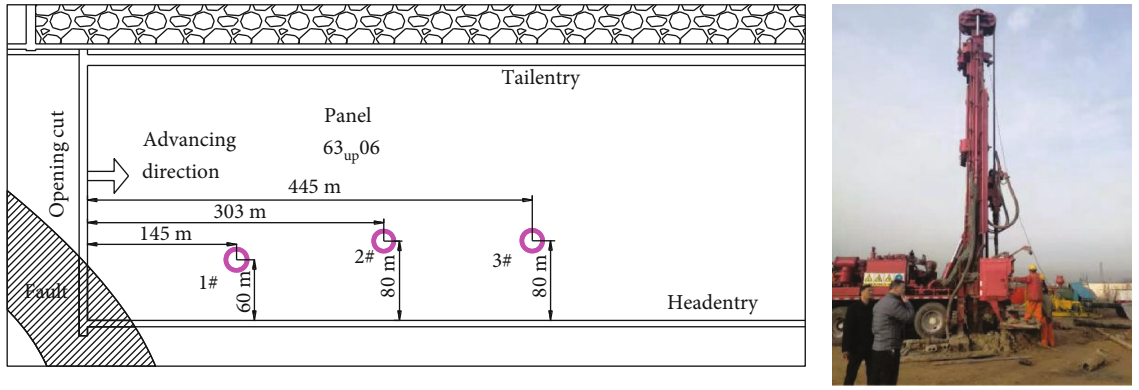

(a) (b)

Figure 18: (a) Schematic diagram of the fracturing layout. (b) Fracturing site.

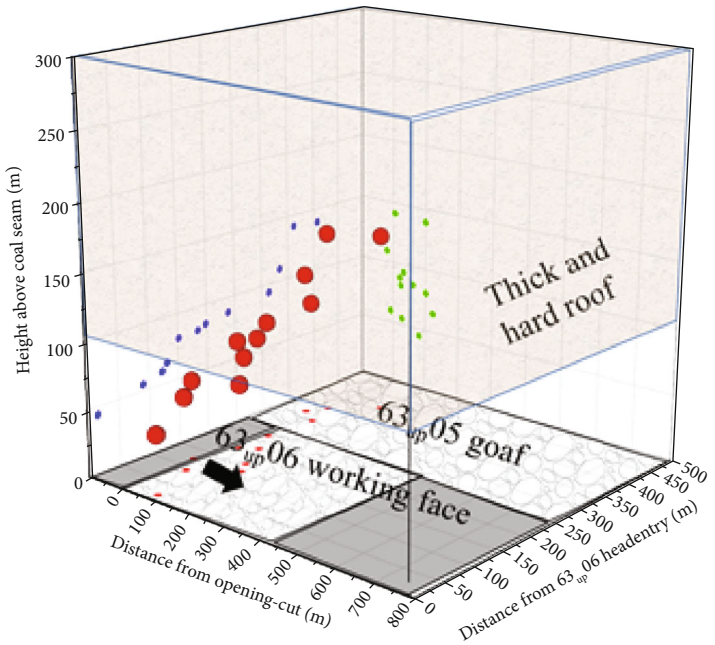

Figure 19: Statistics of high-energy vibration events in the $63_{up}06$ working face.

were arranged along the strike direction of the working face. The microseismic event after fracturing shows that in the direction perpendicular to the formation, the hydraulic fracture has completely cut the THR 100 m above the working face. The expansion direction of the main fracture is shown by the red dotted line in Figure 18(a), which is consistent with the direction of the maximum principal stress. Considering that the THR near the $63_{up}05$ goaf above the working face has been fractured, it can be considered that this fracturing test has fully fractured the high-position THR.

During the first 400 m of the $63_{up}06$ working face mining, 702 microseismic events occurred in total, including 12 high-energy vibration events which include 4 mine earthquakes of magnitude 2.0 and 8 mine earthquakes of magnitude 1.0-2.0, while 35 mine earthquakes of magnitude 2.0 or above occurred in the first 400 m of the $63_{up}05$ working face. Although there are still mine earthquake events in the fractured strata after mining, the frequency of high-energy events was significantly reduced compared with that of the adjacent mined working face. Figure 19 is the specific location diagram of the high-energy mine earthquake event in the working face. The mining earthquake events are mainly concentrated in the rear of the working face and near the opening cut, and there was no high-energy mining earthquake event in front of the working face. Therefore, the engineering field experiment shows that the ground fracturing can effectively prevent the occurrence of high-energy vibration events in mines and ensure the efficient and safe production of coal mining enterprises.

6. Conclusion

In this study, the ground fracturing technology was proposed to cut the high-position THR in advance to control

and prevent mine earthquake. Taking the $63_{up}06$ working face as the engineering background, the movement law of high-position THR before and after fracturing was studied by using FLAC numerical simulation. Then, the fracturing test was carried out in the $63_{up}06$ working face. Several conclusions were obtained as follows.

(1) According to the FLAC simulation, the tensile failure runs through the whole THR and generated an integral fracture; when THR reaches the first breaking span, the THR bottom subsidence preceded the middle and upper parts, and the THR subsidence value closed to the opening cut was higher than that far away from the opening cut. The THR fracture is related to the continuous upward transfer of horizontal compressive stress, which results in the concentration of horizontal compressive stress in THR. Therefore, overcoming the concentration of horizontal compressive stress can effectively alleviate the dynamic disaster caused by the large-area overall breaking of the thick rock stratum

(2) After fracturing, the first breaking span of THR was obviously reduced, and different fracturing positions have a great impact on the THR fracture form. When the fracturing position is closed to the opening cut, the THR presents an overall cantilever beam breaking form and deviates to one side of the goaf, which may cause some potential safety hazards. When the fracturing position is close to the center of the first breaking span, the THR breaks on both sides of the top and sinks along the hydraulic fracture in the middle, and the collapse degree is relatively uniform

(3) During the first 400 m of the $63_{up}06$ working face mining after fracturing, 702 microseismic events occurred in total, including 12 high-energy vibration events which include 4 mine earthquakes of magnitude 2.0 and 8 mine earthquakes of magnitude 1.0-2.0. Compared with the adjacent working face, the quantity of high-energy mine earthquake events in the 63up06 working face has been significantly controlled. The mining earthquake events are mainly concentrated in the rear of the working face and near the opening cut, and there was no high-energy mining earthquake event in front of the working face

Data Availability

The data used to support the findings of this study are available from the corresponding author upon request.

Conflicts of Interest

The authors declare that there is no conflict of interest.

Acknowledgments

The research described in this paper was financially supported by the Key Research and Development Project of Shandong Province in China (2019SDZY02) and the National Natural Science Foundation Project of China (U1762216, 51974353, and 51991362).

References

[1] N. Jiang, C. X. Wang, H. Y. Pan, D. W. Yin, and J. B. Ma, "Modeling study on the influence of the strip filling mining sequence on mining-induced failure," *Energy Science & Engineering*, vol. 8, no. 6, pp. 2239–2255, 2020.

[2] J. Zhou, M. Koopialipoor, E. Li, and D. J. Armaghani, "Prediction of rockburst risk in underground projects developing a neuro-bee intelligent system," *Bulletin of Engineering Geology and the Environment*, vol. 79, no. 8, pp. 4265–4279, 2020.

[3] B. Hebblewhite and J. Galvin, "A review of the geomechanics aspects of a double fatality coal burst at Austar Colliery in NSW, Australia in April 2014," *International Journal of Mining Science and Technology*, vol. 27, no. 1, pp. 3–7, 2017.

[4] J. Ma, N. Jiang, X. Wang, X. Jia, and D. Yao, "Numerical study of the strength and characteristics of sandstone samples with combined double hole and double fissure defects," *Sustainability*, vol. 13, no. 13, Article ID 7090, 2021.

[5] Y. Tan, H. Cheng, S. Gong et al., "Field study on the law of surface subsidence in the high-intensity fully mechanized caving mining working face with shallow thick bedrock and thin epipedon in hilly areas," *Advances in Materials Science and Engineering*, vol. 2021, no. 13, Article ID 6515245, 13 pages, 2021.

[6] Q. Gao, Y. F. Cheng, S. C. Han, C. L. Yan, and L. Jiang, "Numerical modeling of hydraulic fracture propagation behaviors influenced by pre-existing injection and production wells," *Journal of Petroleum Science and Engineering*, vol. 172, pp. 976–987, 2019.

[7] Q. Gao, S. C. Han, Y. F. Cheng, C. L. Yan, Y. W. Sun, and Z. Y. Han, "Effects of non-uniform pore pressure field on hydraulic fracture propagation behaviors," *Engineering Fracture Mechanics*, vol. 221, article 106682, 2019.

[8] M. Dietz, G. M. Oremek, D. A. Groneberg, and M. H. K. Bendels, "What is a rock burst?," *Zentralblatt für Arbeitsmedizin, Arbeitsschutz und Ergonomie*, vol. 68, no. 1, pp. 45–49, 2018.

[9] A. Fakhimi, O. Hosseini, and R. Theodore, "Physical and numerical study of strain burst of mine pillars," *Computers and Geotechnics*, vol. 74, pp. 36–44, 2016.

[10] M. C. He, L. E. Sousa, T. Miranda, and G. L. Zhu, "Rockburst laboratory tests database - application of data mining techniques," *Engineering Geology*, vol. 185, pp. 116–130, 2015.

[11] Y. C. Xue, T. Xu, W. C. Zhu, H. Zhen, and X. W. Wang, "Full-field quantification of time-dependent and -independent deformation and fracturing of double-notch flawed rock using digital image correlation," *Geomechanics and Geophysics for Geo-Energy and Geo-Resources*, vol. 7, no. 4, pp. 1–15, 2021.

[12] Q. Gao, S. C. Han, Y. F. Cheng, Y. Li, and Z. Y. Han, "Apparent permeability model for gas transport through micropores and microfractures in shale reservoirs," *Fuel*, vol. 285, article 119086, 2021.

[13] T. Yi, X. Han, Y. Weitao et al., "Study on the overburden failure law of high-intensity mining in gully areas with exposed

bedrock," *Frontiers in Earth Science*, vol. 10, article 833384, 2022.

[14] A. T. Iannacchione and S. C. Tadolini, "Occurrence, predication, and control of coal burst events in the US," *International Journal of Mining Science and Technology*, vol. 26, no. 1, pp. 39–46, 2016.

[15] G. Banerjee and A. K. Ray, "Singh GSP hard roof management-a key for high productivity in longwall coal mines," *Journal of Mines, Metals and Fuels*, vol. 51, no. 7-8, pp. 238–244, 2016.

[16] A. Keneti and B. Ainsbury, "Review of published rockburst events and their contributing factors," *Engineering Geology*, vol. 246, pp. 361–373, 2018.

[17] M. Ghorbani, K. Shahriar, M. Sharifzadeh, and R. Masoudi, "A critical review on the developments of rock support systems in high stress ground conditions," *Journal of Mining Science and Technology*, vol. 30, no. 5, pp. 555–572, 2020.

[18] I. Vennes, H. Mitri, D. R. Chinnasane, and M. Yao, "Large-scale destress blasting for seismicity control in hard rock mines: a case study," *International Journal of Mining Science and Technology*, vol. 30, no. 2, pp. 141–149, 2020.

[19] C. Xu, L. Yuan, Y. P. Cheng, K. Wang, A. T. Zhou, and L. Y. Shu, "Square-form structure failure model of mining-affected hard rock strata: theoretical derivation, application and verification," *Environmental Earth Sciences*, vol. 75, no. 16, 2016.

[20] H. Liu, B. Yu, J. Liu, and T. Wang, "Investigation of impact rock burst induced by energy released from hard rock fractures," *Arabian Journal of Geosciences*, vol. 12, no. 12, 2019.

[21] T. Zhao, C. Y. Liu, K. Yetilmezsoy, S. Zhang, and S. Zhang, "Fractural structure of thick hard roof stratum using long beam theory and numerical modeling," *Environmental Earth Sciences*, vol. 76, no. 21, 2017.

[22] J. L. Jia, L. W. Cao, D. J. Zhang et al., "Study on the fracture characteristics of thick-hard limestone roof and its controlling technique," *Environmental Earth Sciences*, vol. 76, no. 17, 2017.

[23] D. X. Chen, C. Sun, and L. G. Wang, "Collapse behavior and control of hard roofs in steeply inclined coal seams," *Bulletin of Engineering Geology and the Environment*, vol. 80, no. 2, pp. 1489–1505, 2021.

[24] Q. M. Zhang, E. Y. Wang, X. J. Feng, Y. Niu, L. Song, and H. Wang, "Rockburst risk analysis during high-hard roof breaking in deep mines," *Natural Resources Research*, vol. 29, no. 6, pp. 4085–4101, 2020.

[25] Y. W. Lan, R. Gao, B. Yu, and X. B. Meng, "In situ studies on the characteristics of strata structures and behaviors in mining of a thick coal seam with hard roofs," *Energies*, vol. 11, no. 9, 2018.

[26] Z. P. Guo, W. Q. Mou, W. P. Huang, and H. Q. Duan, "Analysis on roadside support method with constant resistance yielding-supporting along the goaf under hard rocks," *Geotechnical and Geological Engineering*, vol. 34, no. 3, pp. 827–834, 2016.

[27] J. X. Zhang, B. Y. Li, N. Zhou, and Q. Zhang, "Application of solid backfilling to reduce hard-roof caving and longwall coal face burst potential," *International Journal of Rock Mechanics and Mining Sciences*, vol. 88, pp. 197–205, 2016.

[28] B. X. Huang, Q. Y. Cheng, X. L. Zhao, W. C. Xue, and M. Scoble, "Using hydraulic fracturing to control caving of the hanging roof during the initial mining stages in a longwall coal mine: a case study," *Arabian Journal of Geosciences*, vol. 11, no. 20, 2018.

[29] W. L. Zhang, X. C. Qu, C. Li, S. L. Zhang, G. D. Jin, and Y. L. Wang, "Fracture analysis of multi-hard roofs based on microseismic monitoring and control techniques for induced rock burst: a case study," *Arabian Journal of Geosciences*, vol. 12, no. 24, 2019.

[30] C. Li, H. P. Xie, M. Z. Gao, J. Xie, G. D. Deng, and Z. Q. He, "Case study on the mining-induced stress evolution of an extra-thick coal seam under hard roof conditions," *Energy Science & Engineering*, vol. 8, no. 9, pp. 3174–3185, 2020.

[31] J. W. Liu, C. Y. Liu, Q. L. Yao, and G. Y. Si, "The position of hydraulic fracturing to initiate vertical fractures in hard hanging roof for stress relief," *International Journal of Rock Mechanics and Mining Sciences*, vol. 132, article 104328, 2020.

[32] Y. Zhao, B. Q. Lin, T. Liu, and W. Yang, "Influence of hard-roof on gas accumulation in overlying strata: a case study," *Journal of Natural Gas Science and Engineering*, vol. 90, article 103948, 2021.

[33] Y. X. Sun, Y. K. Fu, and T. Wang, "Field application of directional hydraulic fracturing technology for controlling thick hard roof: a case study," *Arabian Journal of Geosciences*, vol. 14, no. 6, 2021.

[34] B. Yu, J. Zhao, and H. T. Xiao, "Case study on overburden fracturing during longwall top coal caving using microseismic monitoring," *Rock Mechanics and Rock Engineering*, vol. 50, no. 2, pp. 507–511, 2017.

[35] B. Yu, R. Gao, T. J. Kuang, B. J. Huo, and X. B. Meng, "Engineering study on fracturing high-level hard rock strata by ground hydraulic action," *Tunnelling and Underground Space Technology*, vol. 86, pp. 156–164, 2019.

[36] B. Yu, J. Zhao, T. J. Kuang, and X. B. Meng, "In situ investigations into overburden failures of a super-thick coal seam for longwall top coal caving," *International Journal of Rock Mechanics and Mining Sciences*, vol. 78, pp. 155–162, 2015.

[37] Y. Y. Lu, T. Gong, B. W. Xia, B. Yu, and F. Huang, "Target stratum determination of surface hydraulic fracturing for far-field hard roof control in underground extra-thick coal extraction: a case study," *Rock Mechanics and Rock Engineering*, vol. 52, no. 8, pp. 2725–2740, 2019.

[38] R. Gao, T. J. Kuang, X. B. Meng, and B. J. Huo, "Effects of ground fracturing with horizontal fracture plane on rock breakage characteristics and mine pressure control," *Rock Mechanics and Rock Engineering*, vol. 54, no. 6, pp. 3229–3243, 2021.

[39] R. Gao, T. J. Kuang, Y. Q. Zhang, W. Y. Zhang, and C. Y. Quan, "Controlling mine pressure by subjecting high-level hard rock strata to ground fracturing," *International Journal of Coal Science & Technology*, vol. 8, no. 6, pp. 1336–1350, 2021.

[40] R. Gao, B. J. Huo, H. C. Xia, and X. B. Meng, "Numerical simulation on fracturing behaviour of hard roofs at different levels during extra-thick coal seam mining," *Royal Society Open Science*, vol. 7, no. 1, article 191383, 2020.

[41] C. Pan, B. W. Xia, B. Yu, P. Yu, Y. F. Luo, and Y. G. Gao, "Determination of the key parameters of high-position hard roofs for vertical-well stratified fracturing to release strong ground pressure behavior in extra-thick coal seam mining," *Energy Science & Engineering*, vol. 8, no. 6, pp. 2216–2238, 2020.

[42] C. Xu, Q. Fu, X. Cui, K. Wang, Y. Zhao, and Y. Cai, "Apparent-depth effects of the dynamic failure of thick hard rock strata on the underlying coal mass during underground mining," *Rock Mechanics and Rock Engineering*, vol. 52, no. 5, pp. 1565–1576, 2019.

[43] Y. C. Xue, T. Xu, P. Wasantha, T. H. Yang, and T. F. Fu, "Dynamic disaster control of backfill mining under thick magmatic rock in one side goaf: a case study," *Journal of Central South University*, vol. 27, no. 10, pp. 3103–3117, 2020.

[44] N. Jiang, D. W. Yin, J. B. Ma, H. Liu, H. Y. Pan, and Y. Qian, "Effects of water immersion on the long-term bearing characteristics of crushed gangue in goaf," *Geofluids*, vol. 2021, Article ID 6675984, 11 pages, 2021.

[45] D. Sun, Y. Xue, and Q. Wu, "Numerical investigation on overburden migration behaviors in stope under thick magmatic rocks," *Geomechanics and Engineering*, vol. 22, no. 4, pp. 349–359, 2020.

[46] Itasca Consulting Group, *FLAC 3D (Fast Lagrangian Analysis of Continua in 3-Dimensions) 5.0 Manual*, Itasca Consulting Group, Inc, 2013.

[47] J. W. Park, Y. Guglielmi, B. Graupner et al., "Modeling of fluid injection-induced fault reactivation using coupled fluid flow and mechanical interface model," *International Journal of Rock Mechanics and Mining Sciences*, vol. 132, article 104373, 2020.